Editors' Suggestion

Acoustic Radiation From a Superconducting Qubit: From Spontaneous Emission to Rabi Oscillations

Vijay Jain,[1,2,*] Vladislav D. Kurilovich,[2,3] Yanni D. Dahmani,[1,2] Chan U Lei,[1,2] David Mason,[1,2] Taekwan Yoon,[2,3] Peter T. Rakich,[1,2,†] Leonid I. Glazman,[1,2,3,‡] and Robert J. Schoelkopf[1,2,§]

[1] *Department of Applied Physics, Yale University, New Haven, Connecticut 06511, USA*
[2] *Yale Quantum Institute, Yale University, New Haven, Connecticut 06511, USA*
[3] *Department of Physics, Yale University, New Haven, Connecticut 06511, USA*

(Received 23 January 2023; revised 26 April 2023; accepted 18 May 2023; published 11 July 2023)

Hybrid quantum systems that utilize controllable coupling between phonons and superconducting qubits could pave the way for a new generation of compact quantum memories and sensor technologies. However, the same electromechanical interaction mechanisms that enable coherent qubit-phonon coupling can also lead to decoherence due to the spontaneous phonon emission. In this paper we study the dynamics of a qubit coupled to an acoustic resonator by a piezoelectric film. By varying the surface topography of the resonator from rough to flat to shaped, we explore the crossover from fast decay of an excited qubit to quantum-coherent coupling between the qubit and an isolated phonon mode. The developed theoretical model allows us to establish and check quantitative links between the results obtained for the rough and shaped topographies. Discrepancy between the theory and the data for the flat resonator points to the imperfections of the studied device. Our experimental approach may be used for precision measurements of crystalline vibrations, the design of quantum memories, and the study of electromechanical contributions to dielectric loss.

DOI: 10.1103/PhysRevApplied.20.014018

I. INTRODUCTION

Circuit quantum electrodynamics (cQED) is a versatile platform for universal quantum computation [1–3] and the design of hybrid quantum architectures [4]. Fast, multicavity control is enabled by a transmon qubit's large electric dipole moment, which can strongly couple to several microwave modes simultaneously [5]. In the emerging domain of quantum acoustics, a superconducting qubit can efficiently couple to collective vibrations—phonons—to prepare nonclassical states of sound and coherently exchange quantum excitations [6–12]. Given that the speed of sound is much slower than that of light, phonons in crystalline media may form a high-density quantum random access memory in a compact form factor with a transmon serving as a nonlinear mixing element to interface multiple acoustic modes [13]. However, coupling a qubit to an acoustic medium with many degrees of freedom can lead to rapid decay if the modes are either very lossy or if coupling to a continuum of modes produces unintended acoustic radiation.

The spontaneous emission rate of a quantum emitter is determined by the density of states (DOS) in the environment. According to Fermi's golden rule, the decay rate γ of a two-level system from spontaneous emission reflects the DOS $D(\omega)$ at its transition frequency ω and its coupling rate g to those states, or $\gamma = 2\pi|g|^2 D(\omega)$. A transmon qubit in free space would have a submicrosecond lifetime because its large size makes it an efficient radiator to the electromagnetic continuum. However, embedding the qubit in a high Q-factor microwave cavity suppresses the continuum DOS by several orders of magnitude when the qubit is strongly detuned from the cavity resonance [14]. This leads to an inverse Purcell effect [15], where the qubit is protected from radiative decay such that other nonradiative mechanisms begin to dominate.

Before we can utilize phonons as a resource for compact quantum acoustic memories and sensor technologies, it is necessary to suppress unintentional acoustic radiation of the qubit into a continuum of modes typically supported by macroscopic systems. In quantum acoustic devices, qubits are coherently coupled to surface and bulk acoustic waves and to phononic defect cavities using piezoelectric materials [16–19]. While strong coupling has enabled single-phonon control, the lifetimes of qubits in current piezo devices can be up to 2 orders of magnitude lower than those of conventional transmons [20]. Since the qubit

*vijay.jain@yale.edu
†peter.rakich@yale.edu
‡leonid.glazman@yale.edu
§robert.schoelkopf@yale.edu

footprint is much larger than the acoustic wavelength, it may potentially radiate into the acoustic continuum. This problem is common for the devices designed to support a coherent superposition of the qubit excitation and an acoustic resonator mode, and for the cQED qubits with nominally passive dielectric substrates. To better understand such qubit decoherence pathways, it can be helpful to identify the dynamics associated with electromechanical coupling of a qubit to the phonon modes hosted by an acoustic resonator.

In this work we investigate acoustic radiation of a transmon with piezoelectric transducers on a high overtone bulk acoustic wave resonator (HBAR) made of a thin film of aluminum nitride (AlN) on sapphire. By modifying the surface topography, we systematically vary the acoustic density of states (ADOS) and explore three unique regimes of acoustic radiation. First, we couple the qubit to a resonator with a roughened backside and observe that the qubit's lifetime shortens by 2 orders of magnitude; see Sec. II A. Disorder on the scale of the acoustic wavelength makes the qubit irreversibly emit its energy into a continuum of phonon modes. Next, by coupling the qubit to a flat acoustic resonator, we observe a modulation of its lifetime that is consistent with discrete bands in the expected ADOS; see Sec. II B. Finally, by shaping the piezoelectric transducer, we form acoustic bound states whose spectral signatures we observe in the qubit's decay (see Sec. II C) and to which we can coherently couple (see Sec. II D).

In parallel, we develop a theoretical model describing a qubit coupled to the acoustic modes in HBAR. We determine the parameters of the model using the data for the resonator with a roughened backside, see Sec. II A, and then use it to predict the experimental results for all the other studied geometries. We find a very good agreement with the data for shaped transducers; see Secs. II C and II D. There are substantial deviations of the data for the flat resonator from the theoretical predictions; see Sec. II B. The discrepancy can not be explained by deviations of HBAR from flat geometry and points to device imperfections which are undetermined at this stage.

II. MEASURING ACOUSTIC RADIATION

To study acoustic radiation, we track the dynamics of a flux-tunable qubit as a function of frequency when coupled to different acoustic environments. Our experimental platform consists of a flip-chip assembly, in which one chip contains the qubit and its metallic traces and the other the HBAR. The qubit has a concentric capacitor layout that shunts a pair of parallel Josephson junctions, resulting in a transition frequency at approximately $\omega_0/2\pi = 5$–6 GHz. Flux threading the square loop is used to tune the qubit's frequency over a broad range; strong, off-resonant voltage drives are used to quickly Stark shift the qubit's frequency in a narrow range. An adjacent meandering

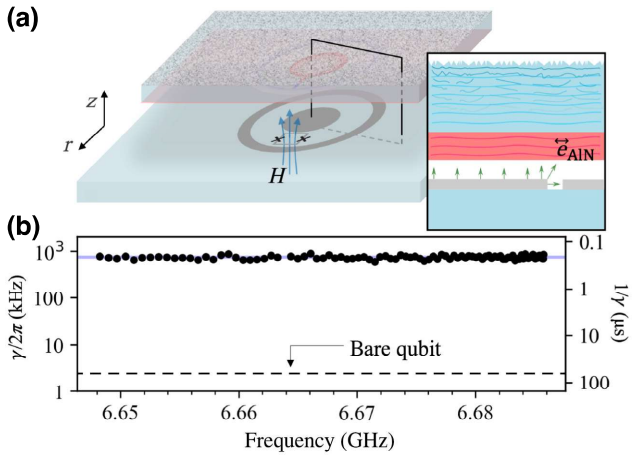

FIG. 1. Acoustic spontaneous emission from a transmon. (a) An illustration of the sample geometry. Stacked above the center of the concentric transmon is a chip with 1 μm of aluminum nitride on 430 μm of sapphire, which has a roughened backside. The chip entirely covers the qubit. An external magnetic field H is applied (field lines in blue) to flux tune the qubit. (Inset) The electric field of the transmon mode excites an acoustic wave in the resonator, via the piezoelectric effect in AlN. The wave scatters diffusely at the roughened backside. (b) The measured qubit decay rate γ is independent of its transition frequency, confirming the diffuse nature of phonon scattering off a rough surface. A blue solid line indicates the analytical estimate using Eq. (1) with $e_{33} = 0.52\ \mathrm{C/m^2}$, and a dashed line shows the decay rate of a control qubit $\gamma_{\mathrm{ctrl}}/2\pi = 2.6$ kHz.

stripline is hanger coupled to a transmission line for dispersive readout. The HBAR is formed from sapphire with a film of aluminum nitride $b_p = 1$ μm thick; aluminum spacers are deposited to form a 1-μm vacuum gap between the qubit and the piezoelectric film. The assembly is mounted in a superconducting package at the base of a dilution refrigerator.

We conduct experiments using three different styles of HBARs that systematically vary the ADOS. First, we use a single-side polished sapphire chip with thickness $b =$ 430 μm, whose backside has a roughness of approximately 1-μm rms [shown in Fig. 1(a)]. Next, we repeat the same with a $b = 100$ μm double-side polished sapphire chip. Finally, we make two separate samples, in which a $b = 100$ μm thick sapphire chip is patterned with an aluminum nitride cylinder of diameter 250 μm or a dome formed through a vapor-phase reflow process [21] and dry etching of the residual piezoelectric.

A. Radiation into acoustic free space

To understand the impact of acoustic radiation on qubit coherence, we begin by investigating the coupling of the qubit to a quasicontinuum of phonon modes. Here, we employ a HBAR with a roughened backside, with roughness on the order of the acoustic wavelength. A qubit is

first brought into the excited state with a fast pulse. Field oscillations within the excited qubit couple (via the piezoelectric effect) to an acoustic wave that traverses the bulk and diffusely scatters from the roughened back surface. Hence, this acoustic excitation does not coherently return to the transducer, leading to spontaneous emission analogous to that of a qubit coupled to acoustic free space. Indeed, measurement results shown in Fig. 1 reveal a fast decay time of $T_1 = 0.21$ μs that does not depend on the qubit's frequency in a 40 MHz bandwidth (a resonator with the same nominal thickness would have a 13 MHz free spectral range). By comparison, a control qubit, which lacks the top HBAR chip entirely, has a lifetime $T_1 = 62$ μs. Therefore, acoustic spontaneous emission is the dominant source of decoherence, occurring at a rate $\gamma/2\pi = 750$ kHz.

We model the roughened HBAR as an acoustic half space to analytically estimate the radiation rate. The main contribution to the spontaneous emission rate in our device comes from the emission of longitudinal waves. The coupling between the qubit and a longitudinal phonon $\hbar g = -\int d^3\boldsymbol{r}\,\sigma_{zz}(\boldsymbol{r})s_{zz}(\boldsymbol{r})$ is determined by the overlap of stress $\sigma_{zz}(\boldsymbol{r}) = e_{33}E_z(\boldsymbol{r})$ generated by the qubit's electric field E in the piezoelectric film, and strain $s_{zz}(\boldsymbol{r}) = s_0 e^{i\boldsymbol{k}_\perp\cdot\boldsymbol{r}_\perp}\sin(k_z z)$ associated with the phonon. Here, e_{33} is the piezoelectric modulus of AlN and s_0 is the zero-point strain amplitude. Applying Fermi's golden rule, we find that [22]

$$\gamma_{\rm fs}(\omega_0) = \frac{2\pi}{\hbar}\frac{4e_{33}^2}{\pi v_l \rho\omega_0}\sin^4\left(\frac{\omega_0 b_p}{2v_l}\right)\int d^2\boldsymbol{r}_\perp E_z^2(\boldsymbol{r}_\perp), \quad (1)$$

where $\rho = 4\cdot 10^3$ kg/ m^3 is the density of sapphire and $v_l = 11.1$ km/s is the longitudinal wave velocity. In the derivation we assumed that the electric field does not change appreciably across the thickness of the piezoelectric film. To find $E_z(\boldsymbol{r}_\perp)$, we use a high-frequency simulation software, which gives $\int d^2\boldsymbol{r}_\perp E_z^2(\boldsymbol{r}_\perp) = 5.2\cdot 10^{-10}$ V^2. For a thin film with $b_p \ll \lambda_{\rm ac}$, the decay rate $\gamma_{\rm fs} \propto (\omega_0/v_l)^3$, analogous to radiation by a dipole in free space. In our experiment, however, the piezoelectric film thickness b_p is close to half the acoustic wavelength ($\lambda_{\rm ac}/2 = 0.9\,\mu$m) at the qubit's transition frequency, yielding $\sin(\omega_0 b_p/(2v_l)) \approx 1$.

The estimate for $\gamma_{\rm fs}$ depends sensitively on the value of the piezoelectric modulus e_{33}, which we have not measured independently. Upon using in Eq. (1) the value $e_{33} = 1.4$ C / m^2 previously reported for polycrystalline AlN thin films [23,24], we find that $\gamma_{\rm fs} = 2\pi\cdot 5.9$ MHz. While this estimate agrees with the measured rate within an order of magnitude, it nonetheless overestimates the experimentally observed rate by a factor approximately equal to 7. We can bring the theory and the data into agreement if we use $e_{33} = 0.52$ C / m^2. Although this value is lower than that for thin AlN films at room temperature (by a factor of approximately 2.5), it is close to the e_{33} extracted from measurements of the coherent coupling to a discrete phonon mode in other quantum acoustic devices [8].

The large difference between the lifetimes of a control qubit ($T_1 = 62$ μs) and a qubit in the roughened HBAR structure ($T_1 = 0.20$ μs) verifies the impact of acoustic spontaneous emission on coherence. This disparity could be even more dramatic in other quantum acoustic designs. From the participation ratio, $p_r = \epsilon_0\epsilon\int \mathrm{d}V E_z^2/\hbar\omega$, we estimate that the qubit stores 1% of its electrical energy in the piezoelectric film. Alternate designs with stronger in-film electric field strengths or piezoelectric coupling e_{33} may cause the qubit's lifetime to drop to nanosecond timescales.

B. Flat acoustic resonator

Next, we consider the qubit coupled to a flat acoustic resonator. We begin with the theoretical predictions for this geometry. If the qubit size, a, is large compared with the acoustic wavelength, we may first dispense with the diffraction phenomena and consider a simplified problem. In it, the qubit couples to a single standing wave in a finite-size resonator of thickness, b, built on top of the qubit footprint. This coupling would result in Rabi oscillations of the excitation between the qubit and acoustic mode. The oscillation frequency depends on the coupling strength, g_0. The Rabi frequency $\Omega_R = 2g_0$ at the resonance of the qubit with the standing wave, $\omega_0 = \omega_n$. The oscillations amplitude is of the order of 1 for $|\omega_0 - \omega_n| \lesssim g_0$.

Diffraction modifies this picture. To account for diffraction, one needs to treat the HBAR chip as a thick multimode waveguide that supports bands of phonon modes. The wave spectrum in it, $\omega_n^2(k_\perp) = v_l^2(n\pi/b)^2 + v_\perp^2 k_\perp^2$, is characterized by the in-plane wave vector $k_\perp$ and the standing wave overtone number n. The subset of wave vectors $k_\perp$ of phonons efficiently interacting with the qubit are limited by diffraction to $k_\perp \lesssim \pi/a$. The respective mode frequencies $\omega_n(k_\perp)$ form narrow intervals of width $\omega_{\rm diff} \sim v_\perp^2\pi^2/(\omega_n a^2)$ adjacent to the standing wave frequencies $\omega_n = \pi n v_l/b$. The strong-coupling regime requires $g_0 \gg \omega_{\rm diff}$, and is realized close to the resonance, $|\omega_0 - \omega_n| \lesssim g_0$. In the latter frequency range, we predict (see Ref. [22] for details) the presence of damped Rabi oscillations. The decay of the excited qubit happens in two stages. The first stage corresponds to the decay of the Rabi oscillations; the decay rate is $\gamma_R \sim \sqrt{g_0\,\omega_{\rm diff}}$. By the end of this stage, the excited-state population decreases by a factor of 4 from its initial value. Further relaxation of the qubit occurs slower and without oscillations.

The size $a \sim 100\,\mu$m of the qubit determines the diffraction width of $\omega_{\rm diff}/2\pi \sim 10$ kHz. Using the value of the piezoelectric constant extracted from the data in Sec. II A,

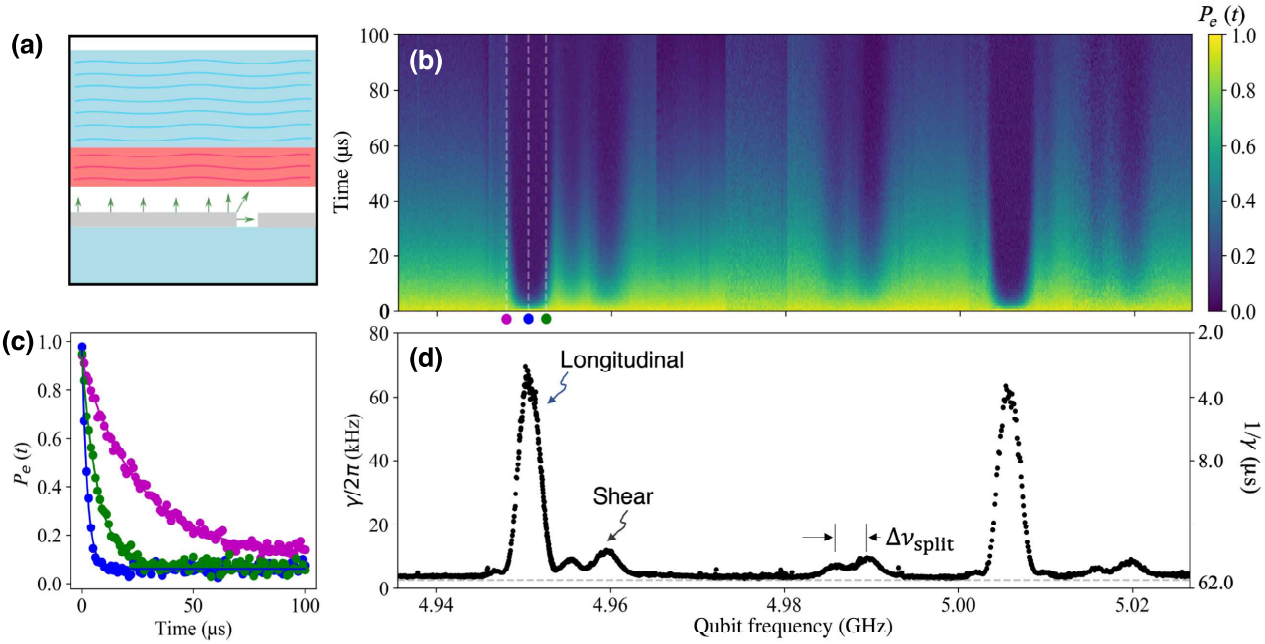

FIG. 2. Dynamics of the qubit coupled to a flat acoustic resonator. (a) As opposed to the inset of Fig. 1, the backside of the acoustic resonator is flat. (b) Time dependence of the excited-state population of the qubit $P_e(t)$ at different qubit frequencies ω_0 ($P_e(t)$ is shown with the color). (c) Line cuts of the plot in panel (b) at three different qubit frequencies. Data points in blue, green, and magenta correspond to the frequencies indicated in panel (b) with circles of the respective colors. The time dependence of $P_e(t)$ is well described by a single decaying exponent (solid lines). (d) Measured decay rate $\gamma(\omega_0)$ of the qubit at each frequency. The gray dashed line is the decay rate of the control sample γ_{ctrl}. The peaks in $\gamma(\omega_0)$ correspond to the resonances between the qubit and the standing acoustic waves.

$e_{33} = 0.52$ C/m^2, we estimate $g_0/2\pi \sim 1$ MHz and, therefore, $\gamma_R/2\pi \sim 100$ kHz. Accordingly, we expect strong qubit-phonon coupling within the frequency range of width of the order of 1 MHz around the resonances $\omega_0 = \omega_n$, and of the order of 10 resolved Rabi oscillations.

Having outlined the theoretical predictions, we now turn to the data. The results for the dynamics of a qubit coupled to a flat resonator are shown in Fig. 2. First, we observe a periodic structure of prominent peaks in the qubit decay rate. The free spectral range between the peaks, $v_l/(2b) = 55.5$ MHz, corresponds to round-trip travel time of the longitudinal wave across the acoustic resonator. The peak widths of the order of 1 MHz are seen in Fig. 2(d). These observed ~ 1 MHz peak widths agree with the prediction of the strong-coupling regime of the qubit-phonon interaction. In fact, the height of the peaks approximately equal to 70 kHz is consistent with $\gamma_R/2\pi \sim 100$ kHz. However, in contrast to the theory prediction, we observed no Rabi oscillation at any qubit frequency; see Fig. 2(b). Instead of the two-staged decay, the time dependence of the excited-state population of the qubit is well described by a single exponential; see Fig. 2(c).

The Rabi oscillations could be destroyed by deviations of HBAR from flat geometry or possible additional sources of the phonon decay. However, these mechanisms would lead to peaks in γ with weights much higher than those observed. A possible resolution is that, in addition to the deficiency of sample geometry, the sample's piezoelectric coupling constant e_{33} is unexpectedly an order of magnitude lower than the value we found in Sec. II A. However, that value, $e_{33} = 0.52$ C/m^2, allows us to quantitatively explain the measurement data for the devices with the shaped transducers (see Secs. II C and II D below). Therefore, the discrepancy between the theory and the data for the device of Fig. 2 still awaits explanation.

To conclude this section, we note that, in addition to the primary series of peaks in the qubit decay rate, there is an extra series of peaks of smaller magnitude, cf. Fig. 2(d). These peaks repeat with the period $v_{\text{sh}}/(2b) = 31$ MHz, corresponding to the round trip of the shear wave (the shear wave velocity is $v_{\text{sh}} = 6.1$ km/s). The shear wave peaks are split into two subpeaks that appear to be consistent to the two shear polarizations. The splitting likely originates from a slight misalignment between the z axis of the device (along which the waves are launched) and the c axis of sapphire crystal. Were the two axes perfectly aligned, the two shear waves would have had the same propagation velocities in the z direction, and identical sets of the standing wave frequencies. The misalignment of these axes by $\Delta\theta$ results in a relative difference of the shear wave velocities and corresponding standing wave frequencies, $\Delta\omega_{\text{split}}/\omega_0 = \Delta v_{\text{sh}}/v_{\text{sh}} \propto \Delta\theta$. We estimate (see Ref.

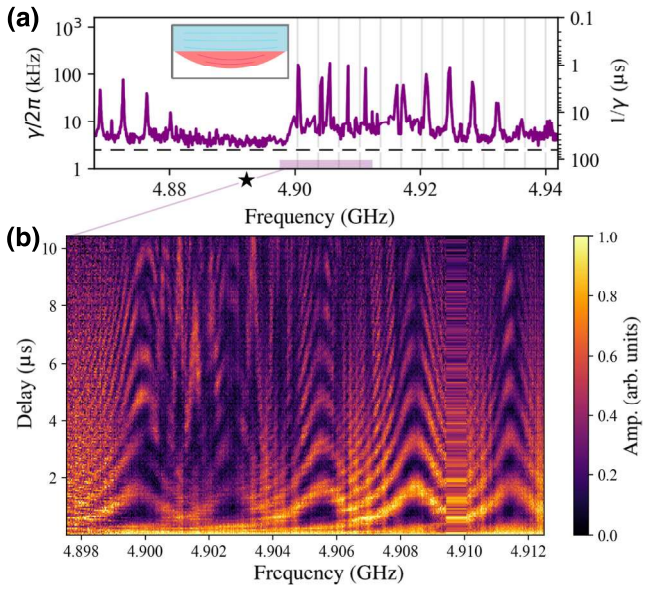

FIG. 3. Dynamics of the qubit coupled to the acoustic modes in the dome. (a) Decay rate of the qubit γ as a function of the qubit frequency. A series of peaks originates from the coupling of the qubit to the (lossy) acoustic modes confined within the dome. Vertical gray lines indicate the calculated mode frequencies; see Ref. [22] for details. A dashed horizontal line shows the decay rate of a control qubit $\gamma_{\mathrm{ctrl}}/2\pi = 2.6$ kHz. (b) When the qubit frequency is close to a resonance with one of the acoustic modes, its excited-state population (depicted with color) undergoes Rabi oscillations.

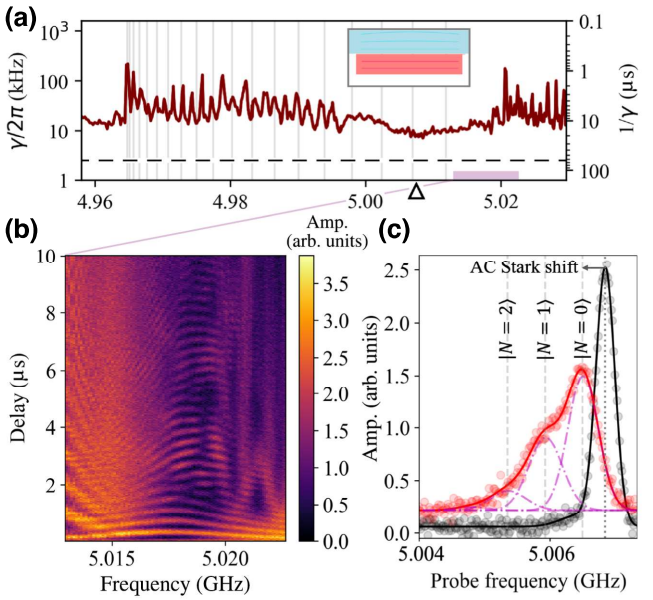

FIG. 4. Dynamics of the qubit coupled to the acoustic modes in the cylinder. (a) The frequency dependence of the qubit's decay rate γ in the cylindrical geometry. We attribute the peaks in γ to the resonances between the qubit and the acoustic modes in the cylinder. (b) The pattern of Rabi oscillations close to the resonance between the qubit and the phonon mode. The decay rate of a control qubit $\gamma_{\mathrm{ctrl}}/2\pi = 2.6$ kHz is shown by a dashed line. (c) A measurement of the dispersive shift of the qubit produced by a driven acoustic mode at $\omega_{\mathrm{ph}}/2\pi = 5.0175$ GHz. The qubit is detuned from the mode by $\Delta/2\pi = -10.5$ MHz; its transition frequency ($\omega_0 = \tilde{\omega}_0 + N\chi$) and linewidth ($\gamma_q = 2\gamma_2 + N\kappa$) depend on the number of excitations N in the displaced acoustic mode [25]. The linewidth of the $|N=1\rangle$ peak is broader than that of the $|N=0\rangle$ peak by $\kappa/2\pi = 21.8$ kHz. The respective acoustic lifetime is $T_1^{\mathrm{ph}} = 7.3$ μs.

[22] for details) that the observed splitting can be explained by a misalignment angle $\Delta\theta = 0.15°$; this estimate is close to the alignment error $\pm 0.1°$ in the specifications of the sample.

Lastly, away from the longitudinal and shear peaks, the decay rate $\gamma/2\pi = 3.4$ kHz is close to that of the control qubit, $\gamma_{\mathrm{ctrl}}/2\pi = 2.6$ kHz.

C. Topographic deformation

Finally, by changing the shape of the acoustic resonator, we create a series of discrete phonon modes that produce a distinctly different spectrum of spontaneous emission. We fabricate two devices with different transducer shapes depicted schematically in Figs. 3(a) and 4(a). In the first device we pattern a dome, etch away the remaining piezoelectric film, and stack it above the center conductor of the qubit. The radius of the dome's base is chosen such that the transducer is slightly smaller than the qubit's center conductor; this reduces the sensitivity of the device performance to the sharply varying fields at the edges of the conductors. The radius of curvature of the dome is $\mathcal{R} = 7.8$ mm. In the second device we pattern a cylinder-shaped transducer with $r = 125$ μm. The measured dependence of the qubit's decay rate on its frequency is presented for both devices in Figs. 3(a) and 4(a).

A striking feature of Figs. 3(a) and 4(a) is the presence of tightly packed peaks in the qubit's decay rate whose spacing $\delta\nu \sim 1$ MHz is much smaller than the fundamental frequency of the bulk standing wave $v_l/(2b) = 55.5$ MHz. We attribute these peaks to the resonances between the qubit and the long-lived acoustic "bound" states. Such bound states (or leaky modes) are formed in the volume of the chip above the transducer by the lateral confinement. To verify the origin of the peaks, we solve the Christoffel wave equation for the two geometries at hand [22], and compare the resulting spectra of bound state frequencies with the positions of peaks in $\gamma(\omega_0)$. For each bulk wave overtone n, we find a series of bound states distinguished by the transverse wave number, with frequency spacing $\delta\nu \ll v_l/(2b)$. The smallness of the spacing stems from the respective smallness of the acoustic wavelength $\lambda_{\mathrm{ac}} \ll \mathcal{R}, b, r$. The computed bound state frequencies are depicted in Figs. 3(a) and 4(a) by the vertical gray lines.

We can also estimate the number of resolvable bound states for each overtone n. Because of the smallness of λ_{ac}, their frequencies, $\omega_n^2(k_\perp) = v_l^2(n\pi/(b+b_p))^2 + v_\perp^2 k_\perp^2$, are accurately estimated by making $k_\perp$ discrete. For example, for the cylindrical transducer, $k_\perp$ changes in steps of width $\sim\pi/r$. The bound states are resolvable as long as the respective frequencies, $\omega_n(k_\perp)$, are lower than the edge of the corresponding overtone's band at frequency, $v_l n\pi/b$. This yields 19 resolved states. A similar calculation for the dome gives 15 resolved states [22]. These numbers are in reasonable agreement with observations.

The decay rate decreases upon detuning the qubit away from the resonances, reaching a minimum background value of 2.8 ($\star$) and 6.6 kHz (Δ) for the dome and cylinder geometries, respectively. Subtracting the control qubit's decay rate, $\gamma_{ctrl}/2\pi = 2.6$ kHz, we find that the contribution of acoustic spontaneous emission is $\gamma_{rad}/2\pi = 0.2$ kHz for the dome geometry and $\lesssim 3.2$ kHz for the cylinder. The elevated radiation from the cylinder stems from the diffraction of acoustic waves in the bulk on the transducer's sharp edge; the dome and its tapered edges, by contrast, suppresses coupling to propagating waves in the bulk. While dielectric losses in the transducer could also contribute to differences from the control, we note that dielectric participation in these two samples is similar, while their γ_{rad} differs by at least an order of magnitude. This verifies that acoustic radiation is more likely than dielectric loss to limit coherence.

D. Acoustic bound state spectroscopy

The discrete nature of the acoustic bound states is confirmed by the presence of multiple vacuum Rabi oscillations in the time domain. Figures 3(b) and 4(b) show the time evolution of the qubit's excited-state population in the dome and cylinder geometries, respectively. In both cases, we observe a clear pattern of vacuum Rabi oscillations. For the dome, the pattern has a standard chevron shape; the oscillations occur at a vacuum Rabi rate, $\Omega_R/2\pi = 0.6$ MHz, when the qubit frequency is tuned to a resonance with the phonon mode, $\omega_0/2\pi = 4.8995$ GHz. By identifying $\Omega_R = 2g$, we infer $g/2\pi = 0.3$ MHz for the qubit-phonon coupling. This value is in good agreement with our estimate, $g/2\pi = 0.24$ MHz, for the qubit interacting with the principal transverse mode in the dome (in the estimate we use $e_{33} = 0.52$ C/m^2 for the piezoelectric coefficient of AlN, as deduced in Sec. II A; see Ref. [22] for details).

For the cylinder, the observed Rabi frequency is $\Omega_R/2\pi = 2.7$ MHz for a phonon mode at $\omega_0/2\pi = 5.0175$ GHz, corresponding to $g/2\pi = 1.35$ MHz for the qubit-phonon coupling. Our analytical estimate for the coupling, $g/2\pi = 1$ MHz, is in reasonable agreement with this value (see Ref. [22] for details). We note that the pattern of oscillations for the cylinder is distorted from its usual chevron shape. This distortion is observed because the high value of the coupling strength, g, is close to the frequency spacing between the bound states, $\delta\nu \sim 1$ MHz, resulting in the hybridization of the qubit with multiple acoustic modes simultaneously.

Next, we find the acoustic bound state decay rate, κ, using the dispersive coupling to the qubit. Here, we focus on a cylindrical geometry. First, by flux tuning the qubit, we park its frequency, ω_0, sufficiently close to ω_{ph}. To enter the dispersive coupling regime, we choose the detuning, $\Delta/2\pi = (\omega_0 - \omega_{ph})/2\pi = -10.5$ MHz, that exceeds $g/2\pi = 1.35$ MHz. Then, we apply a Gaussian pulse resonantly with the bound state, which displaces it into a coherent state—a superposition of Fock states with different phonon numbers N. Because of the dispersive coupling between the qubit and the bound state, $H_{disp} = \chi\sigma_z N/2$, the spectral line in the qubit microwave response becomes a sum of overlapping Gaussians shifted by χ with respect to each other, as seen in Fig. 4(c). The dispersive shift from a single phonon can be evaluated as $\chi = 2g^2/\Delta$, yielding $\chi/2\pi = -0.4$ MHz. The widths of Lorentzians depend on the qubit dephasing rate γ_2, the acoustic bound state decay rate κ, and on the phonon number, $\gamma(N) = 2\gamma_2 + \kappa N$ [25]. The sensitivity of $\gamma(N)$ to phonon number, N, allows us to extract κ by comparing the linewidths corresponding to different N. We fit the shape of the qubit response by a sum of Lorentzians centered at positions $\tilde{\omega}_0 + N\chi$ with widths $\gamma(N)$ ($\tilde{\omega}_0$ differs from ω_0 due to the ac Stark shift induced by the pulse). The only fitting parameters are γ_2, $\tilde{\omega}_0$, and κ. We obtain $\kappa/2\pi = 21.8$ kHz for the decay rate of the bound state, or $T_1^{ph} = 7.3$ μs.

Using this value of κ, we estimate a single-phonon cooperativity $C = 4g^2/(\kappa\gamma_2) = 8.4 \times 10^3$. Its value, which is limited in the present work by dephasing in the qubit $\gamma_2/2\pi = 39.8$ kHz, represents an increase over the previous HBAR devices [8,9], and is the result of an increase in the coupling strength g. Further increase of cooperativity may be achieved by using a transducer with rounded edges (to mitigate the diffraction losses), an acoustic cavity with reduced surface roughness, and a qubit with reduced dephasing.

III. CONCLUSIONS AND OUTLOOK

The speed of sound is 10^4 times slower than that of light; this leads to a high density of acoustic modes in crystalline media as compared with that of electromagnetic modes in a resonator of comparable size. The high density of acoustic modes is both a resource and a challenge for their use in quantum information applications. On the one hand, we may build quantum acoustic devices that are much more compact than existing cQED ones. On the other hand, the higher density of modes may easily lead to a fast decay of a qubit due to the emission of phonons. In this work we demonstrate the crossover between the regime of fast

qubit decay and that of large single-phonon cooperativity; we achieve this by purposefully modifying the device geometry. The relevant length scale for the modifications is determined by the wavelength λ_{ac} of a phonon at the qubit frequency. A surface roughness, of the scale λ_{ac}, within the acoustic cavity results in strong phonon diffraction, which leads to a structureless ADOS mimicking acoustic free space for phonons. In agreement with theory, we observe fast decay of the qubit independent of its frequency, as seen Fig. 1. A surface which is smooth on the scale λ_{ac} limits the spontaneous emission to the set of qubit frequencies resonant with the standing waves in the chip, as seen in Fig. 2. Furthermore, in a full analogy with plano-convex resonators in laser physics [26], shaping of the transducer allows one to isolate discrete long-lived acoustic modes strongly coupled to the qubit. The strong coupling is exemplified by the observed Rabi oscillations, as seen in Figs. 3 and 4.

Our design of the experiments and data analysis went beyond the lumped element circuit models of acoustic modes [27,28] and focused on the wave nature of the coupling. This approach may be extended in several directions. Going forward, we may use it to investigate radiation into Rayleigh waves at the surface. Additionally, we may assess topographic modifications for use in the design of high-density, multimode quantum random access memories based on bulk acoustic wave resonators [13]. Lastly, the technique developed in this work may be used for the precision measurements of the bulk phonon properties, which are hard to access otherwise. For example, we envision the characterization of a weak piezoelectricity caused by defects or the inversion symmetry breaking at the surface [29] of nominally centrosymmetryic crystals. The residual substrate piezoelectricity may contribute to the dielectric loss in qubits.

ACKNOWLEDGMENTS

We thank Luigi Frunzio and Freek Ruesink for valuable discussions and feedback on the manuscript; Yiwen Chu, Konrad Lehnert, Hugo Doeleman, and Uwe von Lüpke for insightful discussions regarding dielectric losses in HBARs; and Nikolay Gnezdilov and Valla Fatemi for initial theoretical discussions. The use of facilities was supported by YINQE and the Yale SEAS cleanroom. This research was initially supported by the U.S. Department of Energy, Office of Science under award number DE-SC0019406 and completed under support by the U.S. Department of Energy, Office of Science, National Quantum Information Science Research Centers, Co-design Center for Quantum Advantage (C2QA) under Contract No. DE-SC0012704. R.J.S. is a founder and equity shareholder of Quantum Circuits, Inc.

[1] A. Wallraff, D. I. Schuster, A. Blais, L. Frunzio, R.-S. Huang, J. Majer, S. Kumar, S. M. Girvin, and R. J. Schoelkopf, Strong coupling of a single photon to a superconducting qubit using circuit quantum electrodynamics, Nature **431**, 162 (2004).

[2] R. J. Schoelkopf and S. M. Girvin, Wiring up quantum systems, Nature **451**, 664 (2008).

[3] A. Blais, A. L. Grimsmo, S. M. Girvin, and A. Wallraff, Circuit quantum electrodynamics, Rev. Mod. Phys. **93**, 025005 (2021).

[4] A. A. Clerk, K. W. Lehnert, P. Bertet, J. R. Petta, and Y. Nakamura, Hybrid quantum systems with circuit quantum electrodynamics, Nat. Phys. **16**, 257 (2020).

[5] Y. Y. Gao, B. J. Lester, Y. Zhang, C. Wang, S. Rosenblum, L. Frunzio, L. Jiang, S. M. Girvin, and R. J. Schoelkopf, Programmable Interference between Two Microwave Quantum Memories, Phys. Rev. X **8**, 021073 (2018).

[6] A. D. O'Connell, M. Hofheinz, M. Ansmann, R. C. Bialczak, M. Lenander, E. Lucero, M. Neeley, D. Sank, H. Wang, M. Weides, J. Wenner, J. M. Martinis, and A. N. Cleland, Quantum ground state and single-phonon control of a mechanical resonator, Nature **464**, 697 (2010).

[7] M. V. Gustafsson, T. Aref, A. F. Kockum, M. K. Ekström, G. Johansson, and P. Delsing, Propagating phonons coupled to an artificial atom, Science **346**, 207 (2014).

[8] Y. Chu, P. Kharel, W. H. Renninger, L. D. Burkhart, L. Franzio, P. T. Rakich, and R. J. Schoelkopf, Quantum acoustics with superconducting qubits, Science **358**, 199 (2017).

[9] Y. Chu, P. Kharel, T. Yoon, L. Frunzio, P. T. Rakich, and R. J. Schoelkopf, Creation and control of multi-phonon fock states in a bulk acoustic-wave resonator, Nature **563**, 666 (2018).

[10] K. J. Satzinger, Y. P. Zhong, H.-S. Chang, G. A. Peairs, A. Bienfait, M.-H. Chou, A. Y. Cleland, C. R. Conner, E. Dumur, J. Grebel, I. Gutierrez, B. H. November, R. G. Povey, S. J. Whiteley, D. D. Awschalom, D. I. Schuster, and A. N. Cleland, Quantum control of surface acoustic-wave phonons, Nature **563**, 661 (2018).

[11] P. Arrangoiz-Arriola, E. A. Wollack, Z. Wang, M. Pechal, W. Jiang, T. P. McKenna, J. D. Witmer, R. V. Laer, and

A. H. Safavi-Naeini, Resolving the energy levels of a nanomechanical oscillator, Nature **571**, 537 (2019).

[12] M. Bild, M. Fadel, Y. Yang, U. von Lüpke, P. Martin, A. Bruno, and Y. Chu, Schrödinger cat states of a 16-microgram mechanical oscillator, arXiv:2211.00449 [quant-ph] (2022).

[13] C. T. Hann, C.-L. Zou, Y. Zhang, Y. Chu, R. J. Schoelkopf, S. M. Girvin, and L. Jiang, Hardware-Efficient Quantum Random Access Memory with Hybrid Quantum Acoustic Systems, Phys. Rev. Lett. **123**, 250501 (2019).

[14] A. A. Houck, J. A. Schreier, B. R. Johnson, J. M. Chow, J. Koch, J. M. Gambetta, D. I. Schuster, L. Frunzio, M. H. Devoret, S. M. Girvin, and R. J. Schoelkopf, Controlling the Spontaneous Emission of a Superconducting Transmon Qubit, Phys. Rev. Lett. **101**, 080502 (2008).

[15] D. Kleppner, Inhibited Spontaneous Emission, Phys. Rev. Lett. **47**, 233 (1981).

[16] U. von Lüpke, Y. Yang, M. Bild, L. Michaud, M. Fadel, and Y. Chu, Parity measurement in the strong dispersive regime of circuit quantum acoustodynamics, Nat. Phys. **18**, 794 (2022).

[17] E. A. Wollack, A. Y. Cleland, R. G. Gruenke, Z. Wang, P. Arrangoiz-Arriola, and A. H. Safavi-Naeini, Quantum state preparation, tomography, and entanglement of mechanical oscillators, Nature **604**, 463 (2022).

[18] G. Andersson, S. W. Jolin, M. Scigliuzzo, R. Borgani, M. O. Tholen, J. C. R. Hernandez, V. Shumeiko, D. B. Haviland, and P. Delsing, Squeezing and Multimode Entanglement of Surface Acoustic Wave Phonons, PRX Quantum **3**, 010312 (2022).

[19] M. Kervinen, A. Välimaa, J. E. Ramirez-Munoz, and M. A. Sillanpää, Sideband Control of a Multimode Quantum Bulk Acoustic System, Phys. Rev. Appl. **14**, 054023 (2020).

[20] M. Scigliuzzo, L. E. Bruhat, A. Bengtsson, J. J. Burnett, A. F. Roudsari, and P. Delsing, Phononic loss in superconducting resonators on piezoelectric substrates, New J. Phys. **22**, 053027 (2020).

[21] P. Kharel, Y. Chu, M. Power, W. H. Renninger, R. J. Schoelkopf, and P. T. Rakich, Ultra-high-Q phononic resonators on-chip at cryogenic temperatures, Appl. Phys. Lett. Photonics **3**, 066101 (2018).

[22] See Supplemental Material http://link.aps.org/supplemental/10.1103/PhysRevApplied.20.014018 for an extended discussion of the experimental design, derivation of the spontaneous emission rate, details of the theory of a qubit coupled to flat and shaped resonators, and material parameters. The Supplemental Material contains additional references [30–37].

[23] M.-A. Dubois and P. Muralt, Properties of aluminum nitride thin films for piezoelectric transducers and microwave filter applications, Appl. Phys. Lett. **74**, 3032 (1999).

[24] M.-A. Dubois and P. Muralt, Stress and piezoelectric properties of aluminum nitride thin films deposited onto metal electrodes by pulsed direct current reactive sputtering, J. Appl. Phys. **89**, 6389 (2001).

[25] J. Gambetta, A. Blais, D. I. Schuster, A. Wallraff, L. Frunzio, J. Majer, M. H. Devoret, S. M. Girvin, and R. J. Schoelkopf, Qubit-photon interactions in a cavity: Measurement-induced dephasing and number splitting, Phys. Rev. A **74**, 042318 (2006).

[26] A. E. Siegman, *Lasers* (University Science Books, Sausalito, CA, 1986).

[27] P. Arrangoiz-Arriola and A. H. Safavi-Naeini, Engineering interactions between superconducting qubits and phononic nanostructures, Phys. Rev. A **94**, 063864 (2016).

[28] A. Ask, M. Ekström, P. Delsing, and G. Johansson, Cavity-free vacuum-rabi splitting in circuit quantum acoustodynamics, Phys. Rev. A **99**, 013840 (2019).

[29] A. B. Georgescu and S. Ismail-Beigi, Surface Piezoelectricity of (0001) Sapphire, Phys. Rev. Appl. **11**, 064065 (2019).

[30] J. Braumüller, M. Sandberg, M. R. Vissers, A. Schneider, S. Schlör, L. Grünhaupt, H. Rotzinger, M. Marthaler, A. Lukashenko, A. Dieter, A. V. Ustinov, M. Weides, and D. P. Pappas, Concentric transmon qubit featuring fast tunability and an anisotropic magnetic dipole moment, Appl. Phys. Lett. **108**, 032601 (2016).

[31] B. A. Auld, *Acoustic Fields and Waves in Solids* (Krieger Publishing Company, Malabar, FL, 1990), 2nd ed.

[32] M. de Jong, W. Chen, H. Geerlings, M. Asta, and K. A. Persson, A database to enable discovery and design of piezoelectric materials, Sci. Data. **2**, 150053 (2015).

[33] I. L. Guy, S. Muensit, and E. M. Goldys, Extensional piezoelectric coefficients of gallium nitride and aluminum nitride, Appl. Phys. Lett. **75**, 4133 (1999).

[34] S. Muensit, I. L. Guy, and E. M. Goldys, Shear piezoelectric coefficients of gallium nitride and aluminum nitride, Appl. Phys. Lett. **75**, 3965 (1999).

[35] M. de Jong, W. Chen, T. Angsten, A. Jain, R. Notestine, A. Gamst, M. Sluiter, C. Krishna Ande, S. van der Zwaag, J. J. Plata, C. Toher, S. Curtarolo, G. Ceder, K. A. Persson, and M. Asta, Charting the complete elastic properties of inorganic crystalline compounds, Sci. Data **2**, 150009 (2015).

[36] A. Iqbal and F. Mohd-Yasin, Reactive sputtering of aluminum nitride (002) thin films for piezoelectric applications: A review, Sensors **18**, 1797 (2018).

[37] J. B. Wachtman Jr., W. E. Tefft, D. G. Lam Jr., and R. P. Stinchfield, Elastic constants of synthetic single crystal corundum at room temperature, J. Res. Natl. Bur. Stand A Phys. Chem. **64A**, 213 (1960).